Xray structural studies of freely suspended ordered hydrated DMPC multimembrane films

G. S. Smith, E. B. Sirota, C. R. Safinya, R. J. Plano, and N. A. Clark

Related Articles

Reversible and fast shift in reflection band of a cubic blue phase in a vertical electric field
Appl. Phys. Lett. 99, 181119 (2011)

Boundary symmetry-stabilized memory in mono-layered cholesteric capsules
APL: Org. Electron. Photonics 4, 223 (2011)

Boundary symmetry-stabilized memory in mono-layered cholesteric capsules
Appl. Phys. Lett. 99, 153308 (2011)

Optical detection of organic vapors using cholesteric liquid crystals
Appl. Phys. Lett. 99, 073504 (2011)

Experimental assessment of quasi-binary picture of thermotropics: Induced smectic A phase in 7CB–n-heptane system
J. Chem. Phys. 135, 044705 (2011)

Additional information on J. Chem. Phys.

Journal Homepage: http://jcp.aip.org/

Journal Information: http://jcp.aip.org/about/about_the_journal

Top downloads: http://jcp.aip.org/features/most_downloaded

Information for Authors: http://jcp.aip.org/authors

X-ray structural studies of freely suspended ordered hydrated DMPC multimembrane films

G. S. Smith[a]
*Exxon Research and Engineering Co., Annandale, New Jersey 08801
and Department of Physics, University of Colorado, Boulder, Colorado, 80309*

E. B. Sirota, C. R. Safinya, and R. J. Plano
Exxon Research and Engineering Company, Annandale, New Jersey 08801

N. A. Clark
Department of Physics, University of Colorado, Boulder, Colorado 80309

We have performed x-ray scattering studies of freely suspended, thick ($\sim 2\mu$), oriented dimyristoyl–phosphatidyl–choline (DMPC)–water multilamellar films with the emphasis on the ordered phases. These stable films were drawn *in situ* on a triple axis x-ray spectrometer at a controlled, continuously variable temperature (T) and relative humidity (RH). The structure was determined at several temperatures and humidities and a T–RH phase diagram was constructed. We have found that the previously labeled ordered $L_{\beta'}$ phase is in fact three distinct two-dimensional phases differentiated by the direction of chain tilt with respect to the in-plane lattice. The line shapes of the scattering data indicate that a lower limit of ~ 200 Å may be placed on the in-plane chain–chain correlation length, while the chain positions are uncorrelated across the water layers.

I. INTRODUCTION

Stacked bilayer membranes in the phospholipid–water system are studied for both their biological and physical significance. Lipid bilayers are the basic building blocks of living cell membranes; therefore, knowledge of lipid–lipid and lipid–protein interactions is essential to understanding endocytosis, fusion meiosis, and other functions of the living cell. For example, previous work[1–4] has shown that these systems exhibit fascinating physical properties due to the complex interplay between attractive van der Waals and repulsive screened electrostatic, hydration, and entropic forces that exist between two membrane sheets separated by an aqueous medium. Additionally, precisely because of the ability to change the intermembrane distance through solvent dilution, these systems are prototype models for elucidating the nature of phases and transitions in two dimensions and the statistical behavior of fluid and ordered surfaces embedded in three-dimensional space.[4,5]

The structural nature of the phases and the phase diagrams of phospholipids and water has been the topic of many experimental investigations.[6–9] Yet, since the early work of Luzzati[6] and co-workers, essentially the same experimental procedures have been used: a sample of fixed lipid/water concentration (by wt.%) was sealed in a thin walled sample tube and x-ray diffraction studies were performed on these samples as a function of temperature. These experiments showed that the three main phases in the phospholipid–water system are the L_α, $L_{\beta'}$, and $P_{\beta'}$. All three of these phases exhibit a stacked water–bilayer structure with a well-defined repeat spacing d. The distinguishing feature of the structures is the in-plane order of the hydrocarbon chains. The L_α phase is the highest temperature phase of the three

for any given concentration. In this phase, the chains are liquidlike with no regular in-plane structure. In lower temperature phases, the chains are frozen into a nearly all *trans* configuration. In the $L_{\beta'}$ phase, the chains form a closed packed lattice in which the bilayer planes are flat and the chains are tilted with respect to the bilayer normal. In the $P_{\beta'}$ phase, the chains are still frozen and tilted, but the bilayer planes become "rippled" with a long wavelength modulation with a period ~ 120–200 Å.

Much of the detailed information about the nature of the in-plane structure and all of the information about the in-plane and out-of-plane correlations are lost in the x-ray diffraction patterns when studying polycrystalline powders. Therefore, to improve on previous work, we have developed a method[10] by which we can produce and study oriented, freely suspended films of DMPC and water. Upon drawing, such films spontaneously orient with the bilayer planes parallel to the film's surface. These films are drawn in a temperature controlled oven in which the chemical potential of water is controlled by an external humidity system. This technique allows us to determine the in-plane structure as well as the d spacing for any value of temperature (T) and relative humidity (RH) between 0 and 80 °C and 0% and 100%, respectively.

We have used our methods to study the detailed structure and correlations within the $L_{\beta'}$ phase (DMPC). To date, it has been thought that the $L_{\beta'}$ phase is well understood. In fact, we find that the $L_{\beta'}$ actually consists of three distinct phases, each distinguished by the direction of the chain tilt with respect to the position of its in-plane nearest neighbors. We find that there are no positional correlations across the water layers; hence, these phases are shown not to be three dimensional in nature, but two-dimensional structures. In addition, the in-plane correlations are found to be relatively short range (~ 200 Å) which suggest a hexatic,

but our in-plane line shapes are also consistent with a two-dimensional solid with finite size domains.

The paper is organized as follows: Section II gives a detailed description of the two-stage film oven, the associated gas flow system, and the x-ray spectrometer. Section III describes the results associated with the DMPC–water system in the temperature-relative humidity (water partial pressure) phase diagram. Section IV concludes with a discussion of the importance of the results.

II. EXPERIMENTAL

To align polycrystalline DMPC–water samples, we use the freely suspended film technique. This technique was first used to align soap films for optical studies and later[11] applied to the alignment of thermotropic (single component) liquid crystals. The technique consists of simply wiping some of the unoriented sample across a hole in a plate. This forms a film which spontaneously orients as it is being drawn, such that the molecular planes lie parallel to the film surface. Such oriented thermotropic liquid crystal samples are stable over several days. A number of x-ray scattering experiments[12-14] have been performed on these types of samples, the purpose being to elucidate the nature of phases and transitions in low-dimensional systems.

The presence of water in the lyotropic liquid crystals poses an additional problem. The water between the bilayer planes is free to diffuse through the surface. In this case, the film becomes unstable due to water evaporation unless this loss is prevented. This may be done by controlling the amount of water vapor in the air around the sample. We have designed and built an oven and humidity control system with which we can draw stable films at a fixed temperature (T) and relative humidity [where the relative humidity (RH) is defined as $100 \times P / P_0$ where P is the partial pressure of water in the air around the sample and P_0 is the saturation vapor pressure at T].

To produce the aligned samples, the film holder–wiper assembly (Fig. 1) was used. The wiper consists of a 0.125 mm thick Be–Cu sheet. The path taken by the wiper during film production is shown in Fig. 1b. Upon pushing down the plunger, the wiper traverses the solid line and upon releasing the plunger the wiper returns (the film drawing cycle) along the dotted line. This scheme prevents the lipid around the edge of the film hole from being shoveled away whenever the wiper is moving in the downward direction. The holes across which the films are drawn are machined into plates which are mounted on the wiping assembly. These holes were machined to a knife edge to provide a smooth surface for the attachment of the lipid film. Several of these plates were made with either 3.0 and 5.5 mm diameter holes, or a 5 mm × 30 mm rectangular hole in either lexan or aluminum plates. Most of the experiments were performed using a 5.5 mm hole in an aluminum plate.

There are two features built into the holder–wiper assembly which allow easy access to several scattering geometries. The first is the integral rotation stage[15] onto which the film plates are directly mounted. This stage rotates about an axis normal to the surface of the film through an angle defined as χ. This allows the scattering vector to be placed
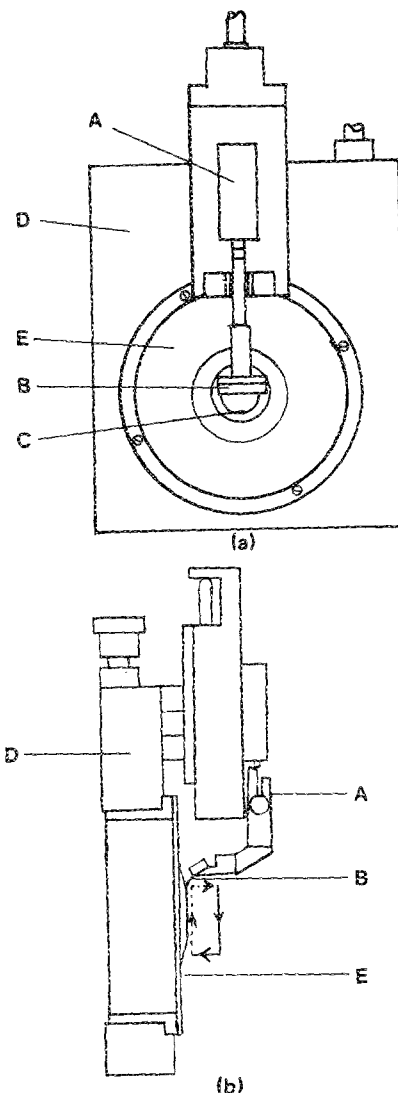

FIG. 1. Film–holder–wiper assembly attached to an Ardel rotary stage. (a) Front view; (b) side view showing the path taken by the wiper. The wiper is spring loaded so that it is only against the holder while moving in the upwards direction. The holder sits in an Ardel Kinematics rotation state to allow rotation about the layer normal. A is the spring loaded wiper assembly, B is the Be–Cu wiper, C is the hole in the aluminum plate across which the film is drawn, D is the Ardel rotary stage, and E is the aluminum holder.

along any in-plane direction. The second feature is in the design of the film holder. Figure 2 illustrates the fact that the plane of the knife edge juts above the rest of the plate. In this way, scattering experiments can be performed such that the beam may be reflected from the film surface at very low angles to probe the interplanar spacings.

The holder–wiper assembly fits into the oven as shown in Fig. 3. This oven has four main functions: (1) it must maintain the film at a constant temperature $-10 \leqslant T \leqslant 80$ °C with a minimum in gradients; (2) it must allow optical observation of the film; (3) it must provide an entrance and exit for the x-ray photons; and (4) the oven must provide a variable humidity environment around the film. To maintain the constant temperature, the oven is constructed of a two stage system of aluminum cans. The outer can acts as a heat shield which is thermally isolated from the inner can. The inner can can either be heated or cooled by a set of seven
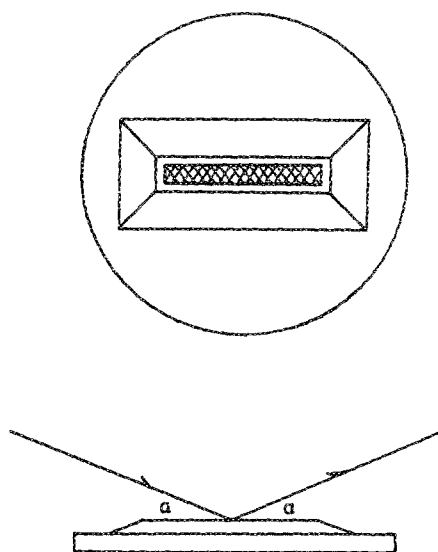
FIG. 2. Rectangular film holder front (top) and side (bottom) views showing how the x rays can reflect from the surface at small angles (α). Stable films were drawn with rectangular dimensions of 5 mm $\times$ 30 mm. A horizontal beam width of 0.5 mm allowed us to access very small reflection angles $\alpha_{min} \sim 0.25°$.

Melcor #CP1.4-31-10L thermoelectric devices (three on the top and four on the bottom, as space permits). These devices are heat sunk to the outer can which can be water cooled. The temperature is measured using YSI 44011 thermistors. Four thermistors on the inner can are used in balancing the temperature to minimize gradients across the sample and as feedback to the temperature controller. Another thermistor is mounted on the χ rotation stage near the sample holder and is used to measure the sample temperature. Using this system, the temperature is controlled with gradients across the film $\leqslant 0.003$ °C/mm.
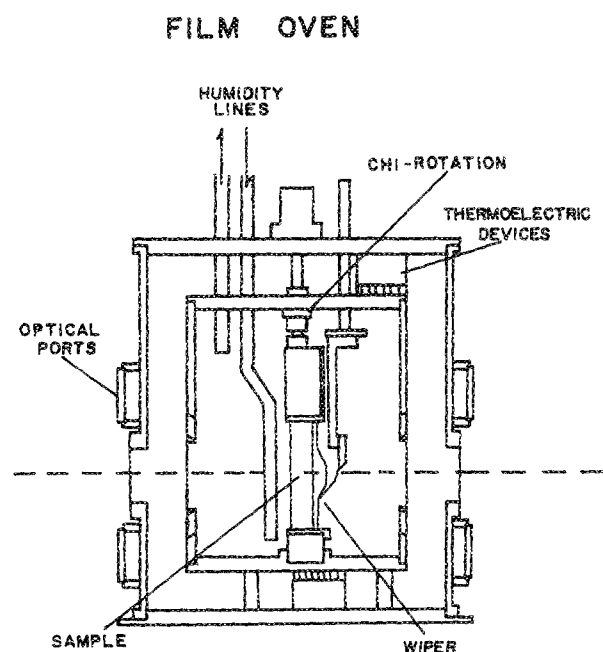
The film may be observed through the optical ports (Fig. 3). These are arranged symmetrically about the center of the oven and allow light to be transmitted through the film or reflected at an angle of 25° with respect to the film normal. The x-ray windows are also shown in the figure. These are made of 0.001-in. thick Dupont aluminized mylar coated with polyester which protects the aluminum from oxidation in a humid environment. These windows have no significant attenuation of the x-ray beam, yet they seal the oven well.

The most important feature of this oven is its ability to maintain a given humidity inside the inner can. To do this, first, all of the cans and feedthroughs are air tight. Then, a source of air with the proper water vapor content is connected to the inlet line shown in Fig. 3. Gently and continuously the gas is flowed through the inner can. The source of the humidified air is an external humidity control system.

The primary function of the humidity control system is to maintain a given water vapor pressure in the air surrounding the sample in the film oven. It does this in a two step process. First, the air in a sealed tank is either moistened or dried to achieve the desired water vapor pressure. Then, this mixture is flowed in a continuous loop between the oven and the tank such that a constant dew point is achieved everywhere. The humidity system consists of a compartmentalized aluminum box. The reservoir contains the gas in which a constant water vapor pressure is maintained. The other end compartment is sectioned into two volumes. One contains water and the other contains silica gel. The central section contains the valves which control the flow of gas from the reservoir to either the water or silica gel. The humidity system is shown schematically in Fig. 4.

Referring to Fig. 4, there are two major loops of gas flow. In one loop, the gas is pumped (both pumps are Cole–

FILM OVEN

HUMIDITY CONTROL SYSTEM

FIG. 3. A schematic of the humidity–temperature controlled (two-stage) oven, described in the text.
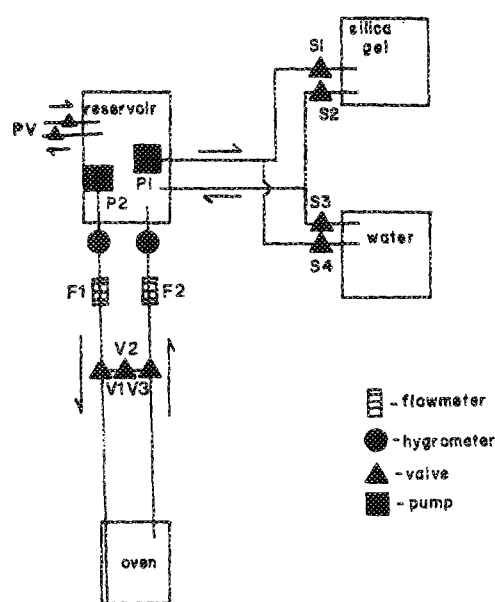

FIG. 4. A schematic of the humidity control gas flow system. See the text for a description of its operation.

Palmer #PD-7088-48 Teflon diaphragm pumps) by $P1$ from the reservoir to the solenoid valves $S1$ and $S4$. If valves $S1$ and $S2$ are open, the gas flows through the silica gel and is dried; whereas, if $S3$ and $S4$ are open, the gas is bubbled through the water bath and is humidified. In either case, the gas is then returned to the reservoir which completes the loop. Pump $P1$ and the solenoid valves only operate if the reservoir water vapor pressure has drifted from the set value. In the second loop, however, the gas is continuously pumped from the reservoir to the oven and back. Immediately after the gas is pumped from the reservoir by $P2$, it passes through a General Eastern model 1200 APS dewpoint hygrometer $H1$. The value of the dew point (which can be converted into the vapor pressure of water) read by $H1$ is used as the value of the dewpoint in the reservoir and is fed back to and compared to the set dew point in the control electronics which operates valves $S1$–$S4$ and pump $P1$. After $H1$, the air passes through $F1$, a minerator flowmeter, with which we can measure the flow of gas to the oven, and in addition, we can dampen the pulsations in the gas due to the diaphragm pump by throttling back the flow using $F1$. If the hand operated valves $V1$ and $V3$ are open and $V2$ closed, the gas then flows to the oven and back. However, if $V1$ and $V3$ are closed and $V2$ open, the gas only flows to and from the reservoir. This is used for trouble shooting and also for equilibrating the system whenever the oven is not attached. On the return route, the gas passes through $F2$ (to measure the return flow) and through $H2$. The dew point read at $H2$ should be the same as the dew point read at $H1$ if no leaks or condensation occur.

Another feature of this sytem is that the aluminum box and all of the components attached to the box are separately temperature controlled with electrical heating tape for operation above room temperature. Also, the flexible stainless steel lines to the oven are heater wrapped and temperature controlled with a YSI controller. This is *necessary* to obtain dew points above room temperature. Water vapor will condense at any point along the path of gas flow at which the temperature is below the dew point. Typically, the temperature of the humidity system and lines is kept a few degrees above the dew point. This system is therefore capable of delivering gas to the oven for which the dew point can be controlled from -20 to $80\,°C$.

The samples were prepared from $>99\%$ pure DMPC powder purchased from Avanti Polar Lipids, Birmingham, Alabama. Prior to drawing the oriented samples, a polycrystalline powder was prepared by mixing the powder with distilled water to form a thin paste. This paste was evenly smeared around the edge of the hole in the film holder which was then mounted inside the oven. The films could only be drawn with the mixture in the L_α phase. Typically this was done at 35° and 90% RH.

In this experiment, we made thick oriented films to study the bulk properties. This required about 0.05 g of the paste ($\sim 30\%$ H_2O) to be placed around the hole. The wiper was driven by a DC motor at a rate which took 5–10 minutes to create a thick film. Photographs of thick films taken in reflection through the upper optical port while shining white light through the bottom port are shown in Figs. 5(b)–5(d). The film appears white (as opposed to colored) because its thickness is significantly greater than the wavelength of visible light, so that the selectivity reflected wavelengths occur at small intervals in λ throughout the visible spectrum (as opposed to just a few selective wavelength reflections in thinner films).[13] The thick films have been removed from the oven in the low temperature $L_{\beta'}$ phase and the thickness was mechanically measured to be $\sim 2\,\mu$. In contrast, we see in Fig. 5(a) a film which shows both white and black (nonreflecting) regions. This is an example of a thick film which partially ruptured leaving a black region whose thickness is on the order of a few bilayers.
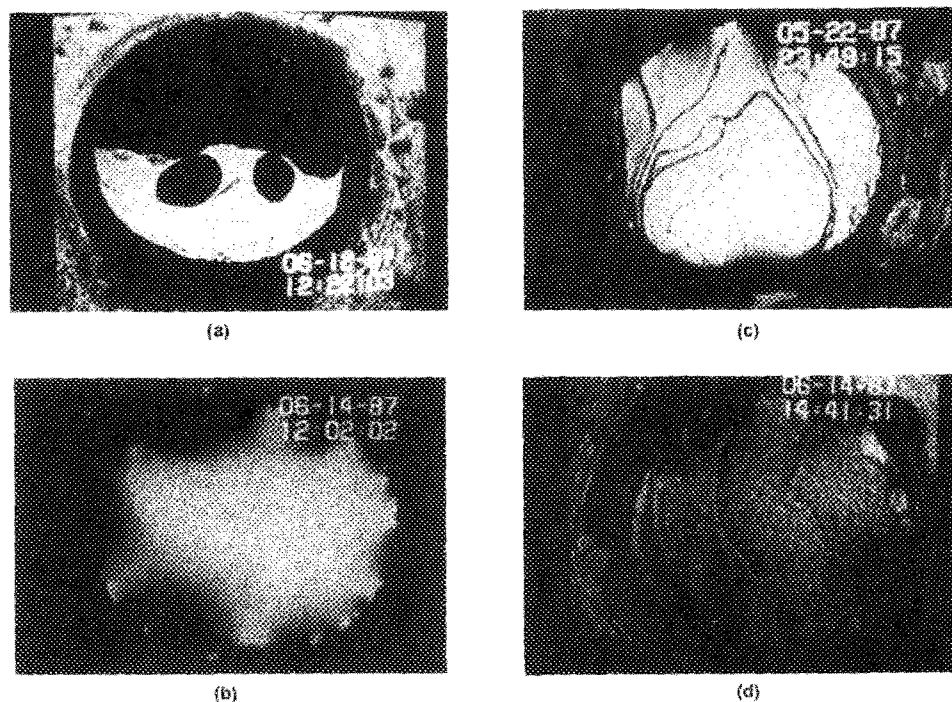

(a)

(c)

(b)

(d)

FIG. 5. Photographs of films taken with unpolarized reflected white light. (b)–(d) are thick films in the (b) L_α, (c) $L_{\beta'}$; and (d) $P_{\beta'}$ phases. (a) A film of nonuniform thickness where that black region is on the order of a few bilayers thick.

To produce films in either the $L_{\beta'}$ or $P_{\beta'}$ phase, we drew a thick L_α film as discussed above. Then we cooled the DMPC to ~ 30 °C while maintaining the humidity at a value near 90%. We then lowered the value of the humidity setpoint to 60–70% and the humidity control system dried the air quickly. From our experience, this is the best procedure to use to ensure that the film neither breaks nor thins. This leaves the film in the $L_{\beta'}$ phase and the temperature and humidity may be adjusted to move to different points in the *T*–Rh phase diagram. To reach the $L_{\beta'}$ phase, a film in the $L_{\beta'}$ phase is hydrated. During these phase transitions, obvious changes take place in the texture of the film in reflected while light. Examples of films in the $L_{\beta'}$ and $P_{\beta'}$ phases are shown in Figs. 5(c) and 5(d), respectively. These changes in texture were of great value in determining the onset of phase transitions and in learning the best ways to cross the phase boundaries.

To perform the x-ray scattering experiments, different combinations of spectrometer components and x-ray sources are used. The first was the low resolution (LR) set-up. In this case, the source of the x-rays was an 18 KW Rigaku RU 300 rotating anode x-ray generator. The Cu K_α line was selected using a focusing pyrolitic graphite (002) monochromator. The in-plane resolution (where "in plane" is defined here as the plane in which the 2θ arm moves) was defined using slits. In this way, the in-plane, longitudinal resolution could be improved over the value of the mosaic of the graphite and it was varied from $\Delta q_{\text{long}} = 0.005$ to 0.013 Å^{-1}; where, $\Delta q_{\text{long}} \simeq (2\pi/\lambda)\cos(2\theta/2)[\Delta(2\theta)]$ and $\Delta 2\theta$ is the full width at half-maximum (FWHM) of a 2θ scan through $2\theta = 0$ or the main beam. The out-of-plane resolution was defined by slits to be $\Delta q_v = 0.1$ Å^{-1}. For the film experiments, the spot size was generally fixed at 1 mm (in plane) wide by 2 mm high (out of plane). The high resolution setup (HR) consisted of a Ge(111) monochromator and analyzer set up at the rotating anode generator. In this case, the out-of-plane resolution was defined by slits with a value of $\Delta q_v \sim 0.1$ Å^{-1}. The in-plane resolution was defined by the Darwin widths of the Ge crystals with a value of $\Delta q_{\text{long}} = 0.000\,56$ Å^{-1}.
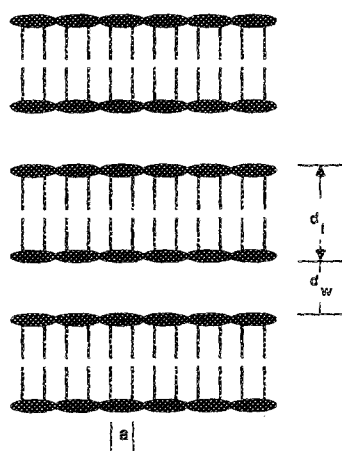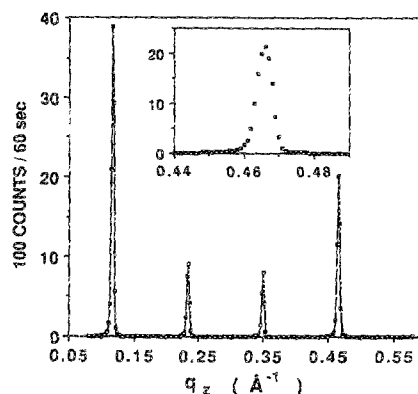

FIG. 7. A q_z scan (reflection) at $T = 31$ °C 90% RH. The fourth harmonic is expanded in the inset.

III. RESULTS

A. *d* spacing

Figure 6 shows the real space configuration of the DMPC–water stacking sequence. The repeat spacing d, of the unit cell along the layer-normal $\hat{z}$ direction is $d_w + d_l$ (water + lipid). The Fourier transform of this real space configuration is simply a series of points along the q_z axis spaced at intervals of $2\pi/d$. Peaks in the scattered x-ray intensity will occur whenever $(k_i - k_f) = (2\pi/d)\hat{z}$. Therefore, reflection geometry scattering must be used to probe the *d* spacing.

We performed a series of x-ray scattering measurements to obtain *d* of a freely suspended film as a function of *T* and RH. A typical scan along the $\hat{q}_z$ axis for a sample at $T = 31$ °C and 90% RH is shown in Fig. 7 where the first four harmonics of the scattering from the bilayer structure can be seen. Several of these scans were performed on a thick film as a function of RH and at constant *T*. A *d* spacing was calculated from the peak position of the fourth harmonic for each scan. (The fourth harmonic was used to minimize any shift in the peak position due to refraction of the x rays as well as to increase sensitivity.) The *d* spacing as a function of RH for several temperatures is plotted in Fig. 8.

The first thing to notice in the figure are the series of discontinuities in the *d* spacing. These represent first order phase transitions. If we plot the position in *T*–RH space of each of these jumps, this maps out the initial *T*–RH phase

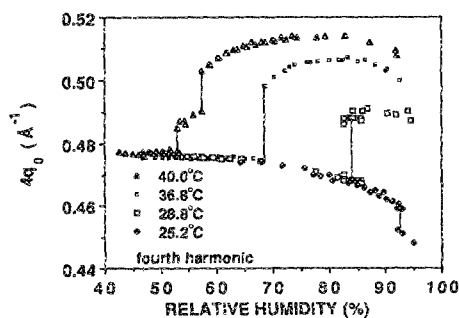FIG. 6. A schematic showing the lipid bilayers. $d = d_{\text{water}} + d_{\text{lipid}}$.

FIG. 8. The peak position ($4q_0$; $q_0 = 2\pi/d$) of the fourth harmonic plotted against RH for four temperatures. The transitions are shown with solid lines. This is one of the ways to map out the phase boundaries.

diagram for this system (see Fig. 18). The three main phases can simply be labeled by comparing their relative positions to one another in this phase diagram to the known T–C (concentration) phase diagram.

In addition to the three main phases L_α, $L_{\beta'}$, and $P_{\beta'}$, we see an indication of a high temperature phase at $T = 40$ °C. This may be the crystalline phase reported by previous studies at low RH.[7]

Another important feature to notice is that while the d spacing of the L_α phase is strongly temperature dependent, there is little or no temperature dependence of d in the $L_{\beta'}$ phase (Fig. 8). This suggests that in the L_α phase some of the d spacing change is due to the changing number of *gauche* bonds, while there is no such change in the $L_{\beta'}$ phase; therefore, the change in bilayer spacing in the $L_{\beta'}$ phase is primarily due to tilting of stiff hydrocarbon chains.

It has been shown that in the L_α phase of DMPC, the dominant force between membranes is the hydration force (F_{hyd}).[1] The microscopic origin of this force is not well understood. It is known, however, to have an experimental dependence on the distance between bilayers of the form

$$f_{\text{hyd}} \sim e^{-d_w/\lambda}, \qquad (1)$$

where d_w is the thickness of the water layer between bilayer membranes (i.e., the membrane separation distance) and λ is the hydration force decay constant which is typically on the order of 2.5 Å. As shown by Parsegian et al.,[1] since the change in the water chemical potential $\Delta\mu$ is the energy required to remove one mole of water from between the bilayers (i.e., the molar Gibb's free energy), $\Delta\mu$ can be divided by the molar volume of water V to obtain

$$\Delta\mu' = \Delta\mu/V = \text{energy/vol} = \text{force/area}. \qquad (2)$$

This is the differential pressure exerted on a bilayer when a volume V of water is removed. In the case of the hydration force, from Eqs. (1) and (2),

$$\Delta\mu' = \Delta\mu_0' e^{-d_w/\lambda}, \qquad (3)$$

the results of the d spacing for the $L_{\beta'}$ phase are independent of T (see Fig. 9), we need to choose only one representative temperature to calculate d vs C. This is shown for $T = 22.5$ °C in the $L_{\beta'}$ phase in Fig. 10. d_w can now be calculated for any point along this curve because the measured value of d gives us the concentration and $d_w = cd$. If we assume that for a given value of d, d_w and d_{lipid} are unique, then we may assign a value of d_w to each value of d for the
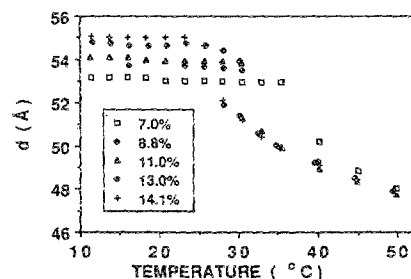

FIG. 10. Layer spacing (d) vs concentration (%H_2O) at $T = 22.5$ °C. The solid line is a least-squares fit to a second order polynomial $d = 54.35 - 0.3600C + .0303C^2$.

vapor pressure data using the bulk sample results. Therefore, we can calculate a value of d_w for each value of RH in the $L_{\beta'}$ phase, and using Eq. (3), we obtain d_w vs $\Delta\mu'$. A plot of $\ln(-\Delta\mu')$ vs d_w is shown in Fig. 11, along with a linear least-squares fit to the data. The fit yields a value of the slope $= -0.487$ Å^{-1} or $\lambda = 2.05$ Å and the intercept gives $\Delta\mu_0' = 3.171 \times 10^9$ dyn/cm^2. This shows that the hydration force is indeed the dominant force in the $L_{\beta'}$ phase.

B. In-plane structure

After defining the phase boundaries among the L_α, $L_{\beta'}$, and $P_{\beta'}$ phases in T–RH space, we performed a series of measurements to investigate the details of the intra-planar molecular structure of the $L_{\beta'}$ phase. For these measurements, transmission geometry x-ray scattering was used. The scattering plane was defined by the vectors q_z and q_r. q_r is a vector lying in the q_x,q_y plane in a direction determined by the polar angle χ, and q_z is perpendicular to the bilayer plane. A set of scans through one of the peaks in the scattered intensity in the $L_{\beta'}$ phase is shown in Fig. 12. Figure 12(a) is a scan at fixed q_r and along the q_z axis. Figure 12(b) is a scan through the peak at fixed q_z along the q_r axis. Figure 12(c) is a scan at fixed q_r and q_z while rotating the film through an angle χ. Figure 12(c) shows that the scattered intensity is constant for any angle χ which is why we can choose an arbitrary q_r vector to define our scattering plane.

To map the constant intensity contours for all of the observed peaks, we performed a series of q_z scans such as in Fig. 12(a) for a set of 16 evenly spaced, fixed values of q_r. The resulting sets of constant intensity contours for

FIG. 9. The layer spacing d vs T from powder samples, sealed in capillaries with fixed amounts of water (% water).
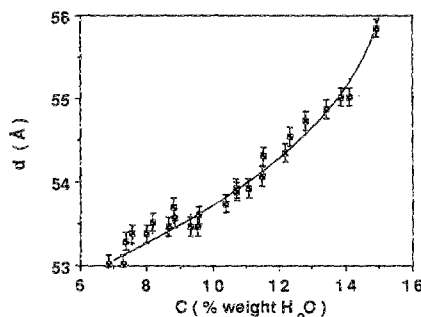
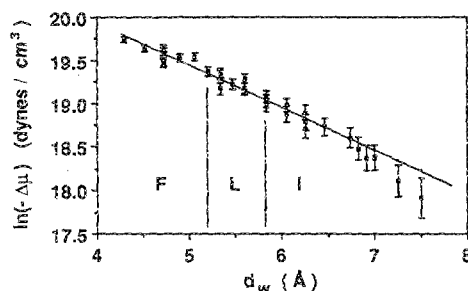

FIG. 11. Computed $\ln(-\Delta\mu)$ vs dw in the $L_{\beta'}$ phases. The fit is to a straight line, showing that hydration is the dominant force.
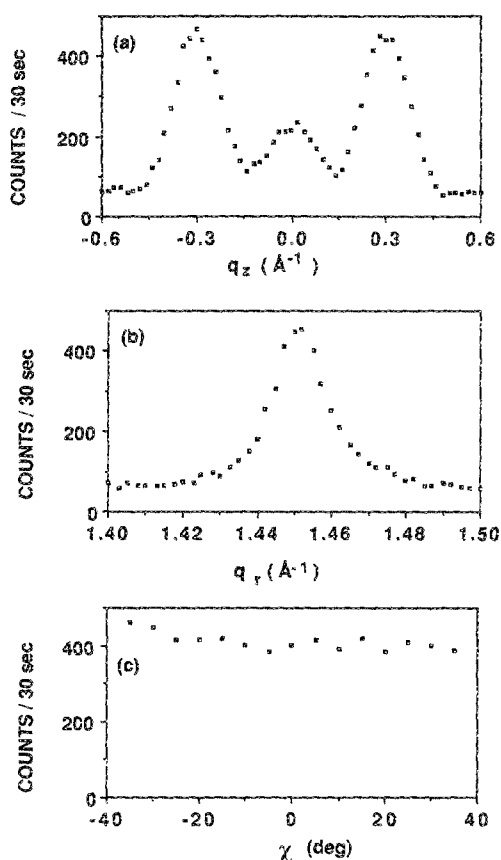
FIG. 12. Scans through in-plane peaks in the $L_{\beta F}$ phase. (a) q_z scan at $q_r = 1.452$ Å^{-1}; (b) q_r scan at the $q_z = 0.3$ peak; (c) χ scan through the peak, showing that there is essentially no alignment within the layer.

$T = 23.5\,°C$ and $RH = 80.4\%$, 83.3%, and 85.9% are shown in Fig. 13. We see that there are three distinct patterns in these constant intensity contours. In each case, there are sets of highest intensity peaks (shown in black) and sets of weaker peaks associated with each of those main peaks.

The peaks may be understood in terms of the interplay between the structure factor and the molecular form factor. If we consider the hydrocarbon tails to be nearly cylindrical in their average charge density, the fundamental harmonic of the form factor which is proportional to the Fourier transform of this charge density has a disk shape in reciprocal space. If the molecule tilts in real space, the form factor (disk) tilts in Fourier space.

To calculate the total structure factor, we need to know the real space lattice. This lattice consists of a single, isolated bilayer of nearly cylindrical hydrocarbon chains on a close-packed distorted triangular lattice. The geometrical structure factor for such a two-dimensional lattice is a set of rods of scattering (not single spots) which form a triangular lattice in reciprocal space. The total structure factor $S(\mathbf{q})$ is given by

$$S(\mathbf{q}) \sim |f(q)|^2 \times \text{geometrical structure factor}, \qquad (4)$$

where $f(\mathbf{q})$ is the form factor for the hydrocarbon chains. Therefore, intensity in the scattering will be observed whenever the x-ray momentum transfer vector is coincidental with the points of intersection of the form factor and the geometrical structure factor. For the case of a set of rods tilted between each other in real space, the intersection of $(f(\mathbf{q}))^2$ and the lattice defines a set of points of scattering. Finally, if the scattering comes from either a set of stacked
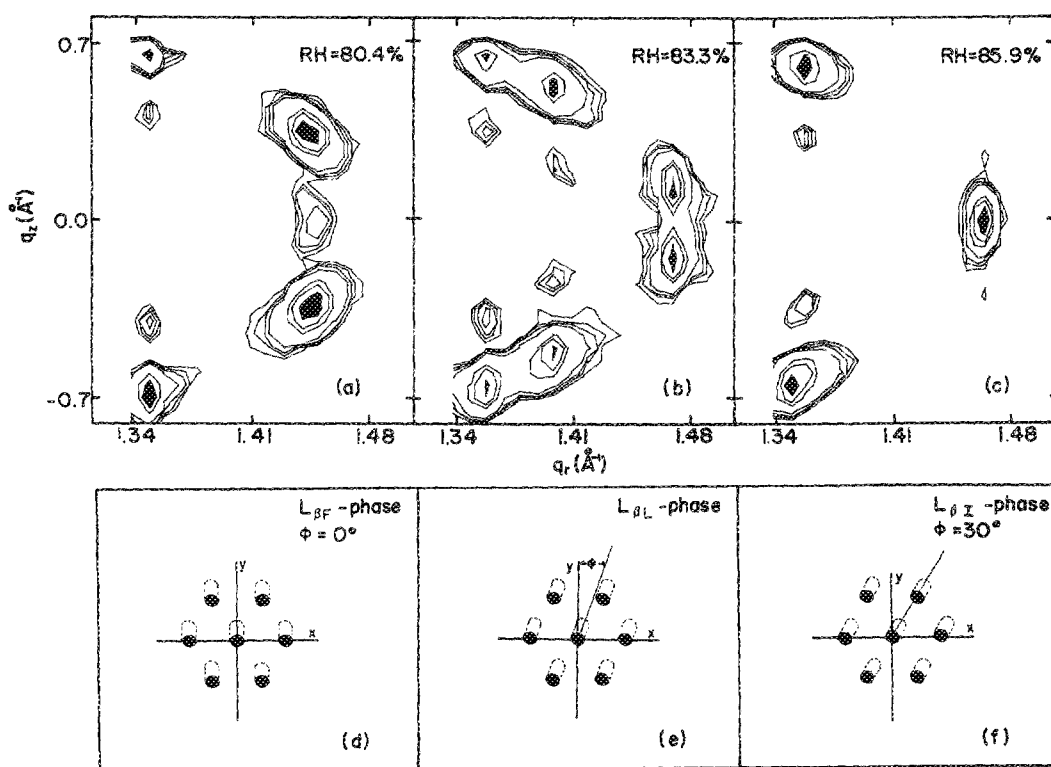

FIG. 13. (a)–(c) q_z vs q_r contour plot of data and (d)–(f) corresponding real space structures of the tail, showing the direction of tilt with respect to the lattice. (a), and (d) 80.0% RH $L_{\beta F}$; (c) and (f) 85.9% $L_{\beta I}$.

and uncorrelated planes, or a set of stacked correlated planes with domains having random in-plane orientations, then the final scattering will be χ powder averaged which is equivalent to a summed rotation of $S(\mathbf{q})$ about the q_z axis. For the case of chains tilted between nearest neighbors, this yields a set of points in the $\mathbf{q}_r, \mathbf{q}_z$ plane as shown in Fig. 13(a). Similarly it can be shown that Fig. 13(c) corresponds to a set of rods tilted toward the nearest neighbor and Fig. 13(b) is for an intermediate case. These real space tilt directions are illustrated below each of the corresponding constant intensity contours in Figs. 13(d)–(f). *This is indeed a remarkable result since the L_β· phase has always been considered to consist of a single structure, where in fact we find that it consists of three different structures distinguished by the relation between the molecular tilt direction and the 2D bond direction. In addition, the middle phase of Fig. 13(b) has never been observed in any other liquid crystal system.* We stress that the three L_β· phases can only be unambiguously distinguished by in-plane scans done in the transmission geometry on well-aligned samples.

The discussion presented above gives the first order explanation of the scattering. To explain the weaker peaks that we see in Fig. 13, we need to model the electronic charge density of the hydrocarbon chains and calculate $S(\mathbf{q})$ as defined in Eq. (4). First we consider the form factor of an untilted chain. We approximate the electronic charge density $\rho(r,z)$ for each chain as a cylindrical charge. Therefore, we can separate $\rho(r,z)$ into $\rho(r)$ and $\rho(z)$. For our cylinder of radius a,

$$\rho(r) = \rho(z), \quad r \leqslant a \tag{5a}$$

$$= 0, \quad r > a. \tag{5b}$$

Since

$$f(\mathbf{q}) \sim \int \rho(\mathbf{r}) e^{i\mathbf{q}\cdot\mathbf{r}} \, d\mathbf{r}^3 \tag{6}$$

and

$$\rho(\mathbf{r}) = \rho(z)\rho(r),$$

then

$$f(\mathbf{q}) = \left[\int \rho(z) e^{iq_z z} dz \right] \frac{2\pi q_r \cdot a}{q_r^2} J_1(q_r a). \tag{7}$$

Our best model for $\rho(z)$ is based on the assumption that most of the in-plane scattering comes from the tails since there is little electronic charge density contrast in the head area. Also it is assumed that the tails are positionally correlated only with other tails within the same bilayer. This model of $\rho(z)$ is shown schematically in Fig. 14 and has the functional form

$$\rho(z) = \rho_1 \frac{(d_2 + z)}{(d_2 - d_1)} \quad -d_2 \leqslant z \leqslant -d_1, \tag{8a}$$

$$\rho(z) = \rho_1 - \rho_2 e^{-z^2/2\sigma^2} \quad -d_1 \leqslant z \leqslant d_1, \tag{8b}$$

$$\rho(z) = \rho_1 \frac{(d_2 - z)}{(d_2 - d_1)} \quad d_1 \leqslant z \leqslant d_2, \tag{8c}$$

where ρ_1 is the difference between the charge density of the tails and the portion of the heads which contribute to the in-plane scattering, ρ_2 is the difference between the charge den-
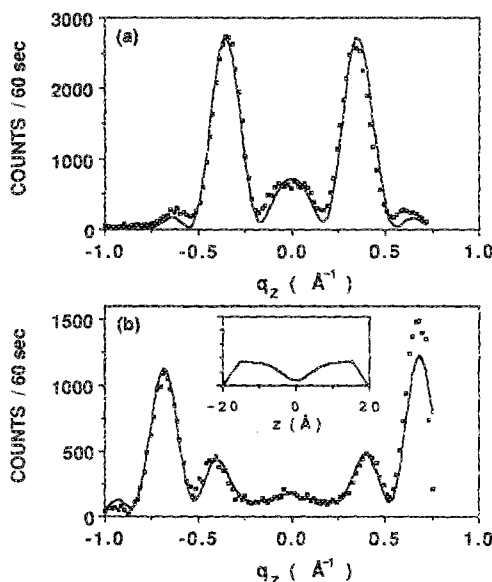

FIG. 14. q_z scans in the $L_{\beta F}$ phase through the 2 q_r peak positions at RH 79%. (a) $q_r = 1.36$ Å^{-1}; (b) $q_r = 1.45$ Å^{-1}. The lines are fits assuming that there are no interlayer correlations where $d_1 = 16.14$ Å, $d_2 = 16.26$ Å, $\rho_1/\rho_2 = 0.44$, and $\sigma = 4.1$ Å. The subsidiary maxima come from the form factor. The mosaic and resolution were much narrower than the features and deconvolution was not necessary. The inset shows the form of charge density (along z), the layer normal used for fits to line shapes.

sity along the chains and the charge density where the chains meet at the center of a bilayer, $(d_2 - d_1)$ is the length of the head group which contributes to the in-plane scattering, d_1 is the length of a single tail, and σ is the width of the section where the tails meet. This form is consistent with the total $\rho(z)$ measured by Torbett and Wilkins[16] and Luzzati.[6] Again, we note that our $\rho(z)$ from the in-plane data is only sensitive to the electron density in the chains.

This model gives the disk shape form factor mentioned above with the addition of higher order modulations along the q_z axis. For the case of tilted molecules, a coordinate transformation (rotation about the appropriate axis) through a tilt angle ϕ must be performed. Then, to get the scattered intensity, we multiply $|f(\mathbf{q})|^2$ by the geometrical structure factor. In this case, for close-packed 2D rods, we get a distorted hexagonal array of long thin rods as the reciprocal lattice. The distortion of the 2D reciprocal lattice from the hexagonal is a contraction along the direction of tilt by a factor of $\cos \theta$.

A fit to the data at $T = 23.5$ °C and RH $= 79\%$, where $d_1, d_2, \rho_1/\rho_2$, and σ are varied is shown in Fig. 14. *The main point to emphasize about these fits is that the peak widths in the q_z direction are described well by the form factor width. This shows that the individual chains are positionally uncorrelated from one bilayer plane to the next.*

Finally, we note that the observation of these three L_β· phases is only possible when the sample is oriented. If the sample is completely polycrystalline as is the case in bulk samples, the observed scattering would be equivalent to powder averaging our data (which is already powder averaged over the azimuthal angle ϕ) over the angle θ such that

$$\langle S(\mathbf{q}) \rangle_{\text{powder average}} = \int_{-\pi/2}^{\pi/2} S(\mathbf{q}) \cos \theta \, d\theta \tag{9}$$

where θ is measured with respect to the q_r axis. We have performed this integration numerically on our data in the $L_{\beta F}$ and $L_{\beta I}$ phases. The results are shown in Fig. 15. This figure emphasizes the fact that the scattering in these different phases are indistinguishable if the sample is polycrystalline.

We can now examine the parameters θ (the chain tilt angle), ϕ (the chain tilt direction), and d as the structure evolves from the $L_{\beta F}$ to the $L_{\beta I}$ phase. Defining

$$\omega_n = \frac{(2\theta)_{\text{peak}}}{2} - \theta_{\text{peak}}, \tag{10}$$

where $(2\theta)_{\text{peak}}$ is the scattering angle of the maximum of each peak and θ_{peak} is the sample rotation away from the normal incidence of the six observed peaks. The six peaks would correspond to the first six $(1,0)$ peaks of the hexagonal lattice looking down the chain axis. In the $L_{\beta F}$ phase, two pairs are degenerate because of the χ averaging of domains. In the $L_{\beta I}$ phase, three pairs are degenerate. In the $L_{\beta L}$ phase, all six peaks are nondegenerate. The index n of the variable ω_n refers to the different peaks. We then find that

$$\cos(\phi + n60°) = \sin \omega_n / \sin \theta, \tag{11}$$

where the azimuthal angle $\phi = 0$ in the $L_{\beta F}$ and $\phi = 30$ in $L_{\beta I}$ phases. To calculate ϕ and θ at each of the values of RH and T, we choose a value of ϕ which minimizes the standard deviation in the values of θ calculated for each of the peaks in the scattering. The results are plotted in Fig. 16 for $T = 23.5$ °C. From the figure, we see that the values of ϕ and θ vary smoothly throughout the $L_{\beta L}$ phase and that within the uncertainty, the transitions from the $L_{\beta L}$ to the $L_{\beta I}$ are not strongly first order and may be second order.

C. In-plane correlations

We have only discussed our data in terms of interplanar correlations. Longitudinal scans through the peaks and parallel to the q_r axis tell us something about the interplanar correlations. Typically we see the same type of results in all three phases; however, to avoid any confusion with contributions to the width from mosaic, we looked specifically at the high humidity $L_{\beta I}$ phase. A longitudinal scan through the on-axis peak in the $L_{\beta I}$ phase at 16 °C and 92% RH is shown in Fig. 17. Shown with this scan is the main beam resolution function of the spectrometer (solid squares). The central

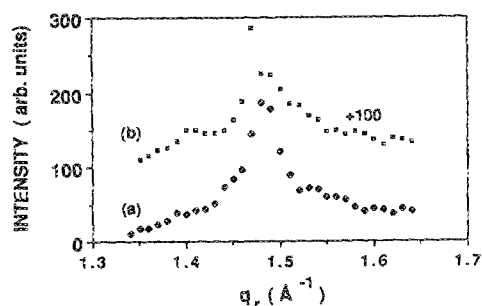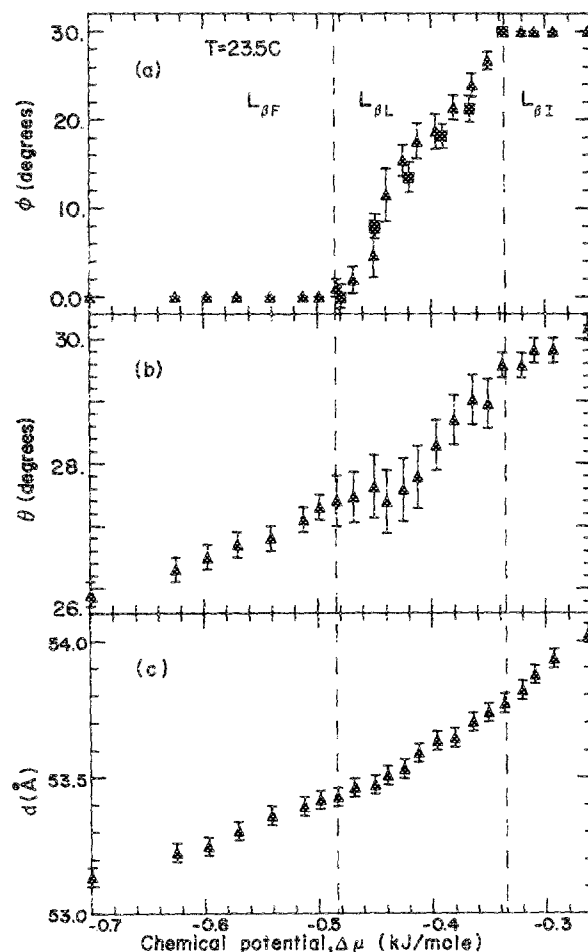FIG. 16. Plot of the (a) azimuthal angle ϕ; (b) tilt angle θ; (c) bilayer repeat distance d vs the chemical potential (derived from the RH) through the $L_{\beta F}$, $L_{\beta L}$, and $L_{\beta I}$ phases. Triangles are taken on hydrating, squares are taken on drying, showing no hysteresis as is expected in second order transitions.

portion of the data has a full width at half maximum of ~ 0.011 Å^{-1} which is larger than the spectrometer resolution width. If the width neglecting the resolution is due to the short range correlations within the plane, then the molecules are correlated over distances of ~ 200 Å. This width may also be due to finite size in-plane domains. It is impossible to reliably differentiate between these two cases without better statistical data taken with a higher resolution spectrometer.
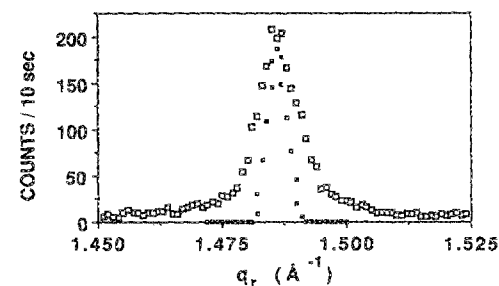

FIG. 15. "Powder average" of the contour data at 28 °C (a) $L_{\beta F}$ 79% RH; (b) $L_{\beta I}$ 86% RH. The differences between these would be subtle and hard to distinguish.

FIG. 17. A q_r scan at $q_z = 0$ in the $L_{\beta I}$ phase at 16 °C 92% RH. The solid squares are the resolution function. Tails are clearly evident showing that there is either a 2D solid with power law tails, or a hexatic giving Lorentzian tails. Higher resolution data would be required to distinguish these possibilities.
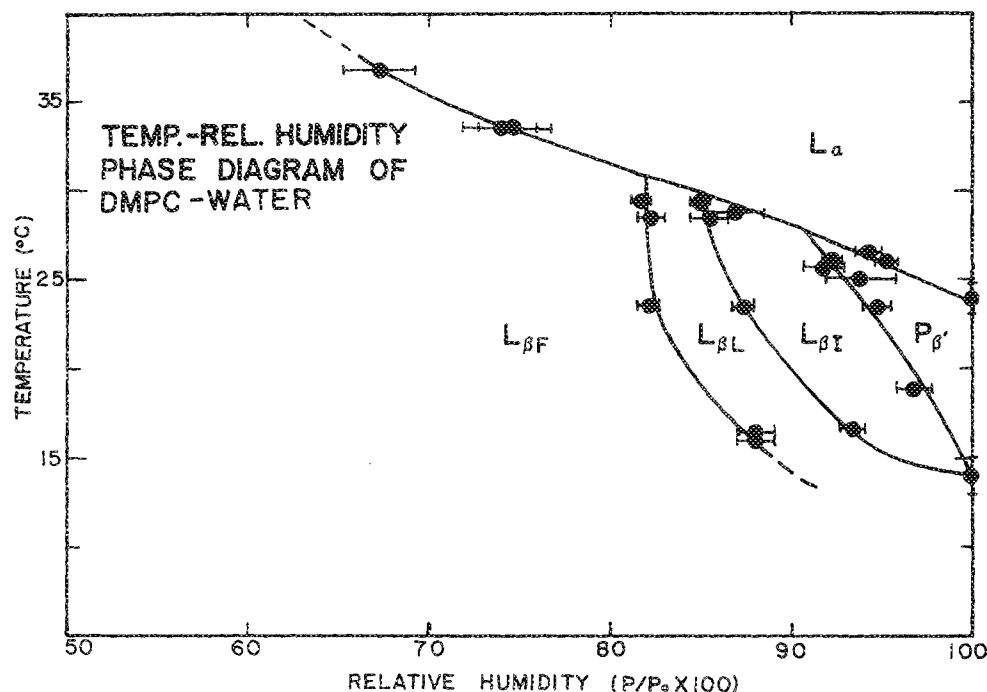
TEMP.-REL. HUMIDITY PHASE DIAGRAM OF DMPC-WATER

FIG. 18. The phase diagram of DMPC-water as a function of temperature and relative humidity, showing the L_α, $P_{\beta'}$ and the newly distinguished $L_{\beta F}$, $L_{\beta L}$, and $L_{\beta I}$ phases. The transitions among the $L_{\beta'}$'s appear second order, while the other transitions are first order.

However, it does allow us to place a lower limit on the in-plane correlations of ~ 200 Å.

In addition to this central peak broadening, the plot shown in Fig. 17 also suggests that the scattering intensity falls slowly for values of q far away from the peak. There are two possible explanations for this. If the system is a 2D hexatic liquid crystal, then we would expect scattering of the form

$$S(\mathbf{q}) \propto \frac{1}{|q - q_0^2| + K^2},$$ (12)

where q_0 is the peak position and κ is the peak width which is inversely proportional to the correlation length. The other possibility is that each bilayer plane is a two-dimensional solid. In this case,

$$S(\mathbf{q}) \propto \frac{1}{|q - q_0|^{2-\eta}}.$$ (13)

We plan experiments to measure these peaks with better statistics and higher resolution using synchrotron radiation, so that we may fit the data to these various forms.

D. The phase diagram of DMPC

We have presented our new x-ray data on the detailed in-plane structure of the $L_{\beta'}$ phase. Using these data and our d-spacing data, we can construct the T-RH phase diagram for the DMPC water system (Fig. 18). As is shown, we have labeled three new phases $L_{\beta F}$, $L_{\beta L}$, and $L_{\beta I}$. The L_β is retained as meaning a lamellar phase in which the molecules are tilted with respect to the bilayer normal. The F and L come from liquid crystal nomenclature, where the F phase is a hexatic liquid crystalline phase, where the molecules tilt between nearest neighbors and the I phase is a hexatic liquid crystalline phase where the molecules tilt toward nearest neighbors. Figure 19 lists the known hexatic, crystalline, and herringbone structures as previously labeled. We have added

a new row to include those structures in which the molecules tilt in a common direction which is neither toward nor between nearest neighbors. We have simply continued the alphabetical labeling, hence, the L, M, and N phases. We have included our structures in the hexatic column. As discussed earlier, we have an indication that these are lower-dimensional systems from the longitudinal scans through the in-plane peaks. Also, since the positional correlations do not extend beyond a single bilayer, it is clear that they are not 3D crystals.

IV. DISCUSSION AND CONCLUSION

As is well appreciated by now, the hydration force is the dominant interaction between neutral phospholipid membranes for small separation distances $5 \leqslant d \leqslant 30$ Å. This strong repulsive potential acts to prevent the approach of phospholipid bilayers embedded in water. A consequence of this interaction is that as the chemical potential of water is increased, the bilayer thickness increases. Our data show that this change in membrane thickness as a function of μ in the $L_{\beta'}$ region is accomplished through a tilt of the frozen hydrocarbon chains. This then results in an increase in the surface area per head group. We point out that the chains on the pseudohexagonal lattice are paired (with the tilt direc-

ϕ	hexatic	crystalline	herring bone
0°	F	G	H
30°	I	J	K
0° $\leqslant \phi \leqslant 30°$	L	M	N

FIG. 19. The extension of the alphabetical nomenclature of tilted layered liquid crystal phases to include phases with the newly discovered intermediate tilt directions.

tion possibly being determined by the average direction of pairing) and a dipole is associated with each. We suggest that the in-plane tilt-direction transitions may be driven by the interfacial dipole–dipole interaction (which varies with the average head–head distance) and the entropy associated with pairing points on a hexagonal lattice.[17]

The transitions among the three $L_{\beta'}$ phases are novel in that the middle $L_{\beta L}$ phase is of lower symmetry (point group C_1) than the surrounding $L_{\beta I}$ and $L_{\beta F}$ which both have the same symmetry (point group C_m). For finite θ, the constraint of close packing of the tails results in two distinct phases with the same symmetry; thus, a direct $L_{\beta F}$–$L_{\beta I}$ transition has to be first order. However, this system can undergo a continuous transition because of the presence of the intermediate phase of lower symmetry, which can have continuous transitions to both phases. We propose ϕ as the order parameter for the $L_{\beta F}$–$L_{\beta L}$ transition, and $30°$-ϕ for the $L_{\beta I}$–$L_{\beta L}$. These transitions can be second order or they may have small first-order jumps (within our error bars).

We plan to investigate charged lipid membrane systems using the free standing technique; in particular, it will be interesting to see whether the three $L_{\beta'}$ phases are found in general also in charged systems. Finally, we mention recent theoretical work by Selinger and Nelson[18] on hexatic-to-hexatic transitions in two-dimensional systems. By considering the coupling between the bond and tilt order parameters, they find three phases with the corresponding tilt symmetries which may indeed correspond to the three distinct $L_{\beta'}$ phases that we have discovered.

ACKNOWLEDGMENTS

[1]V. A. Parsegian, N. Fuller, and R. P. Rand, Proc. Natl. Acad. Sci. **76**, 2750 (1979); A. C. Cowley, N. L. Fuller, R. P. Rand, and V. A. Parsegian, Biochemistry **17**, 3163 (1978).

[2]J. N. Israelachvili, *Intermolecular and Surface Forces* (Academic, Orlando, 1985); J. Mahanty and B. W. Ninham, *Dispersion Forces* (Academic, London, 1971).

[3]C. R. Safinya, D. Roux, B. S. Smith, S. K. Sinha, P. Dimon, N. A. Clark, and A. M. Bellocq, Phys. Rev. Lett. **57**, 2718 (1986); D. Roux and C. R. Safinya, J. Phys. (Paris) **49**, 307 (1988); F. Nallet, D. Roux, and J. Prost, Phys. Rev. Lett. **62**, 276 (1989).

[4]R. Lipowsky and S. Leibler, Phys. Rev. Lett **56**, 2541 (1986); R. E. Goldstein and S. Leibler, *ibid.* **61**, 2213 (1988).

[5]Y. Kantor, M. Kardar, and D. R. Nelson, Phys. Rev. Lett. **57**, 791 (1986); D. R. Nelson and L. Peliti, J. Phys. (Paris) **48**, 1085 (1987); J. A. Aronovitz and T. C. Lubensky, Phys. Rev. Lett. **60**, 2634 (1988); for a broad discussion see *Statistical Mechanics of Membranes and Surfaces*, edited by D. Nelson, T. Piran, and S. Weinberg (World Scientific, New Jersey, 1988).

[6]V. Luzzati, Biol. Membrane **1**, 71 (1968); A Tardieu, V. Luzzati, and F. C. Reman, J. Mol. Biol. **75**, 711 (1973).

[7]M. J. Janiak, D. M. Small, and G. G. Shipley, J. Biol. Chem **254**, 6068 (1979).

[8]G. L. Kirk, S. M. Gruner, and D. L. Stein, Biochemistry **23**, 1093 (1984); G. L. Kirk and S. M. Gruner, J. Phys. **46**, 1985; M. B. Schneider and W. W. Webb, J. Phys. (Paris) **45**, 273 (1984).

[9]S. Doniach. J. Chem. Phys. **70**, (1979); W. K. Chan and W. W. Webb, Phys. Rev. Lett. **46**, 39 (1981); M. Marden, H. L. Frisch, J. S. Langer, and H. M. McConnell, Proc. Natl. Acad. Sci. **81**, 6559 (1984); L. Powers and P. S. Pershan, Biophys. J. **20**, 137 (1977); T. Urabe, S. A. Asher, and P. S. Pershan, Proc. Natl. Acad. Sci. **78**, 4941 (1981); J. B. Stamatoff, W. F. Graddick. L. Powers, and D. E. Moncton, Biophys. J. **25**, 253 (1979).

[10]G. S. Smith, C. R. Safinya, D. Roux, and N. A. Clark, Mol. Cryst. Liq. Cryst. **144**, 235 (1987); G. S. Smith, E. B. Sirota, C. R. Safinya, and N. A. Clark, Phys. Rev. Lett. **60**, 813 (1988); E. B. Sirota, G. S. Smith, C. R. Safinya, R. J. Plano, and N. A. Clark, Science **242**, 1406 (1988).

[11]C. Y. Young, R. Pindak, N. A. Clark, and R. B. Meyer, Phys. Rev. Lett. **40**, 7763 (1978).

[12]D. E. Moncton and R. Pindak, Phys. Rev. Lett. **43**, 702 (1979).

[13]E. B. Sirota, P. S. Pershan, L. B. Sorensen, and J. Collett, Phys. Rev. Lett. **55**, 2039 (1985); Phys. Rev. A. **36**, 2890 (1987); E. B. Sirota, P. S. Pershan, S. Amador, and L. B. Sorensen, Phys. Rev. A **35**, 2283 (1987).

[14]J. D. Brock, A. Aharony, R. J. Birgeneau, K. W. Evans-Lutterodt, J. D. Litster, P. M. Horn, G. B. Stephenson, and A. R. Tajbakhsh, Phys. Rev. Lett. **57**, 98 (1986); J. D. Brock, R. J. Birgeneau, J. D. Litster, and A. Aharony, Phys. Today **42**, 52 (1989).

[15]J. Collett, L. B. Sorensen, P. S. Pershan, and J. Als-Nielsen, Phys. Rev. A **32**, 1036 (1985).

[16]J. Torbett and M. H. F. Wilkins, J. Theor. Biol. **62**, 447 (1977).

[17]E. B. Sirota, J. Phys. (Paris) **49**, 1443 (1988).

[18]J. V. Selinger and D. R. Nelson, Phys. Rev. A **61**, 416 (1988).